

Numerical study of sediment transport above rippled beds under the action of combined waves and currents

MING LI and BRIAN A. O'CONNOR

Department of Engineering, Civil Engineering Building, The University of Liverpool, Liverpool L69 3GQ, UK (E-mail: mingli@liv.ac.uk)

ABSTRACT

To study sediment suspension above ripples under the combined action of waves and currents, a three-dimensional numerical model has been developed based on the use of FLUENT software, and an external sediment transport model. The computer model has been tested against laboratory measurements involving oscillatory wave motion, as well as cases of co-linear waves with following and opposing currents, with satisfactory results. Compared with the situation in which only waves are present (called waves-alone cases), the effects from the steady current on both vortex shedding and sediment suspension above ripples have clearly been revealed by the model results. In particular, the vortices generated in combined waves and currents tend to stay low in the trough area of the ripple and are ejected earlier than those in the waves-alone case at both the ripple crest and trough, which leads to concentration peaks at different phases and with different magnitudes. The model was also applied to a field case from a multi-barred, dissipative beach at Egmond-an-Zee, in the Netherlands, to investigate the influences of a long-shore current on cross-shore sediment transport. The model results show reasonable overall agreement with the field measurements, as well as the important effects of the three dimensional flow structure on the sediment entrainment process close to the ripple surface, which is very difficult to observe in such detail in field studies.

Keywords Coastal boundary layer, coastal morphology, mathematical models, sand ripples, sediment transport, vortex shedding.

INTRODUCTION

The state of knowledge of sand transport above a rippled bed subjected to oscillatory wave motion, combined with a steady or unsteady tidal or other current, is still far from satisfactory due to the complexity of the interacting processes in the wave boundary layer, and has hindered progress in improving methods for sand transport rate prediction in the coastal region. In contrast to a flat bed, the distinctive feature of the oscillatory boundary layer above a rippled bed is the shedding of vortices within each half wave cycle, which enhances the sediment suspension process. A number of experimental studies have been conducted recently in order to study these important mechanisms. For example, O'Donoghue & Clubb (2001) noted the similarity of ripple characteristics due to regular sinusoidal waves and second order Stokes waves with equivalent wave period and root-mean-square values of the near-bed orbital velocity. Faraci & Foti (2001) investigated sand ripple generation under monochromatic and random waves, and suggested that wave irregularity was of less importance to equilibrium ripple geometry. Sistermans (2002) carried out a series of experiments in a large-scale flume to study ripple formation due to random waves with graded sediment and suggested a wave-period-averaged linear distribution of sediment diffusivity through the water column. Direct measurements of sediment suspension above a rippled bed were also reported by Thorne *et al.* (2002) with the aim of defining sediment diffu-

hue & Clubb (2001) noted the similarity of ripple characteristics due to regular sinusoidal waves and second order Stokes waves with equivalent wave period and root-mean-square values of the near-bed orbital velocity. Faraci & Foti (2001) investigated sand ripple generation under monochromatic and random waves, and suggested that wave irregularity was of less importance to equilibrium ripple geometry. Sistermans (2002) carried out a series of experiments in a large-scale flume to study ripple formation due to random waves with graded sediment and suggested a wave-period-averaged linear distribution of sediment diffusivity through the water column. Direct measurements of sediment suspension above a rippled bed were also reported by Thorne *et al.* (2002) with the aim of defining sediment diffu-

sivity throughout the water column under various wave conditions. Van der Werf (2006) investigated wave-induced sand entrainment from asymmetrical vortex ripples in a prototype-scale water tunnel with intra-wave period measurement of sediment concentrations and flow velocities under regular second order Stokes waves.

In order to properly represent the organized momentum exchange and the associated sediment transport due to vortex shedding, a number of numerical models also have been reported in the literature. Two-dimensional (horizontal and vertical space coordinates involved, called herein 2DV) and three-dimensional (3D) numerical boundary layer models have become increasingly popular in recent years due to rapid developments in computing technology (e.g. Sleath, 1984; Sato *et al.*, 1986; Blondeaux & Vittori, 1991; Kim *et al.*, 2000; Malarkey & Davies, 2002; Watanabe *et al.*, 2003; Barr *et al.*, 2004; Eidsvik, 2006). The majority of these studies are, however, restricted to situations involving only waves. A limited number of studies have been carried out for situations involving waves and currents acting together on a bed of mobile sediment, particularly at the field scale (e.g. Andersen & Faraci, 2003). Li & O'Connor (2000) and Li (2004) developed a new 3D boundary layer model to simulate the detailed flow structures and related sediment transport rates in combined waves and currents above a range of different types of bedforms, including ripples and dunes. The model was tested against a range of available laboratory and field measurements for flow situations involving waves, currents, and waves combined with currents and was shown to give good results with respect to both flow characteristics and the sand concentration profile above various bedform shapes. Details of the model verification and validation procedures can be found in Li (2004). Li *et al.* (2006) further tested the model against data on equilibrium bed roughness and spatially-averaged near-bed concentrations also with good results.

In the present study, the Li *et al.* (2006) model has been further tested using measurements of sand transport over vortex ripples, at both laboratory and field scale, to reveal the influence from a steady current on the oscillatory flow structures and the sand entrainment from the sea bed. The formulation of the numerical model is described briefly in The Numerical Model section below while details of the model results and discussion of the test cases are presented in the Model Result section.

THE NUMERICAL MODEL

The boundary layer model of Li *et al.* (2006) simulates 3D flow structures and sediment transport processes above each individual ripple at the sea bed. The Reynolds-averaged fluid momentum equations are solved using the CFD FLUENT software (Dvinsky, 1987). The model can use a range of turbulence closures. However, previous work of Li & O'Connor (2000) has compared different closures with experimental results and found that a Reynolds stress transport model (Launder, 1989) gave realistic results for the low Reynolds number flows encountered within the trough region of the bedforms tested. It should be noted that the closure used standard turbulence model coefficients without any special tuning for each individual case that was tested. In order to represent oscillatory wave motion in the model, an external oscillatory-body-force approach was used, similar to that used in the 2DV model of Fredsøe *et al.* (1999). Near-bed orbital velocity was approximated by second order Stokes' theory as follows:

$$U_{\infty} = U_1 \cos \omega t + U_2 \cos 2\omega t \quad (1)$$

where U_{∞} is the free stream velocity, U_1 and U_2 are the first and second order orbital velocity components, ω is the angular wave frequency and t is time. Details of the U_1 and U_2 velocities used for each test case can be found in Tables 1 and 2. Wave and current interaction for cases involving combined waves and currents was dealt with by adjusting the water surface slope in the model after integration over each wave period.

Once the necessary hydrodynamic information was obtained, the instantaneous suspended sediment concentration was predicted using a 3D mass continuity equation:

$$\begin{aligned} \frac{\partial c}{\partial t} + u \frac{\partial c}{\partial x} + v \frac{\partial c}{\partial y} + (w - w_f) \frac{\partial c}{\partial z} \\ = \frac{\partial}{\partial x} \left(\varepsilon_x \frac{\partial c}{\partial x} \right) \\ + \frac{\partial}{\partial y} \left(\varepsilon_y \frac{\partial c}{\partial y} \right) + \frac{\partial}{\partial z} \left(\varepsilon_z \frac{\partial c}{\partial z} \right) \end{aligned} \quad (2)$$

where c is the concentration of suspended sediment; u , v and w are fluid velocities in the x , y and z directions; w_f is the settling velocity of a sediment particle in the z direction; ε_x , ε_y and ε_z are diffusion coefficients in the x , y and z directions, respectively (taken as the same as the effective viscosity computed from the turbulence

Table 1. Test conditions for Villaret & Perrier (1992) experiments.

Test	T35	T36	T38
Water depth, h (m)	1.1	1.1	1.1
Wave period, T (sec)	1.5	1.5	1.5
Wave height, H (m)	0.232	0.188	0.175
Free stream amplitude, a (m)	0.072	0.058	0.054
First order orbital velocity U_1 (m sec ⁻¹) at 35 cm above the bed	0.3	0.243	0.226
Second order orbital velocity U_2 (m sec ⁻¹) at 35 cm above the bed	0.0	0.0	0.0
Median sand size, d_{50} (mm)	0.09	0.09	0.09
Maximum free stream velocity to current velocity ratio, U_1/U_c	–	1.4	–1.3
Bed form height, Δ (m)	0.007	0.006	0.006
Bed form length, λ (m)	0.048	0.050	0.048
Bed form steepness, Δ/λ	0.15	0.12	0.13

Table 2. Parameters for the Saulter *et al.* (2000) 3D field tests.

Wave peak period, T_p (sec)	9.2
Significant wave height, H_s (m)	0.155
Water depth, h (m)	0.62
Free stream amplitude, a (m)	0.445
First order orbital velocity U_1 (m sec ⁻¹) at 0.18 m above bed	0.35
Second order orbital velocity U_2 (m sec ⁻¹) at 0.18 m above bed	0.095
Long-shore current velocity (m sec ⁻¹)	0.14
Current angle, θ (°)	+90
Median sand size, d_{50} (mm)	0.3
Bed form height, Δ (m)	0.015
Bed form length, λ (m)	0.09
Bed form steepness, Δ/λ	0.17

model), x and y are horizontal coordinates in the cross-shore and long-shore directions, respectively, and z is the vertical coordinate measured upwards from the sea bed.

Periodic boundary conditions are introduced at the side boundaries along the two horizontal axes to represent the fully-developed turbulent flow at each end of the computational domain. At the sea bed, the velocities and turbulent kinetic energy are taken to be zero. A gradient boundary condition similar to the Fredsøe & Deigaard (1992) approach was applied to represent sediment entrainment from the bedform surface:

$$\varepsilon_z \frac{\partial c}{\partial z} = -w_f c_a \quad (3)$$

where c_a is the near-bed reference concentration given by Engelund & Fredsøe (1976), which is applied at $2d_{50}$ above the bedform surface, and d_{50} is the median grain size. At the mean water level, a no-stress boundary condition is used for

the hydrodynamic calculation. The sediment concentration is computed based on a no-flux boundary condition, i.e.:

$$\varepsilon_z \frac{\partial c}{\partial z} = -w_f c \quad (4)$$

The bedform surface is represented as a fixed wall at the bottom of the computational domain; typically three bedforms are included in the model simulation. The skin friction roughness of the bedform surface is specified as $2.5d_{50}$. The sediment fall velocity is computed using the method of Van Rijn (1993). Following Meyer-Peter & Müller (1948), the instantaneous bed load transport rate is computed from the equation:

$$q_b = 8(|\theta| - \theta_c)^{3/2} [(s-1)gd_{50}^3]^{1/2} \frac{\theta}{|\theta|} \quad \text{for } |\theta| > \theta_c \quad (5a)$$

$$q_b = 0 \quad \text{for } |\theta| \leq \theta_c \quad (5b)$$

where q_b is the instantaneous bed load transport rate, θ is the Shields' parameter defined as $\theta = u_f^2 / (s-1)gd_{50}$, s is the relative density of the sediment particles, u_f is the shear velocity at the bed surface and g is the acceleration due to gravity. The critical Shields' parameter also contains a modification to allow for the effects of a sloping bed on initiation of motion.

The fluid momentum and mass conservation equations are solved by the finite volume method with a QUICK (Leonard, 1979) interpolation scheme. The sediment mass conservation equation is solved by an implicit finite difference method on the same curvilinear, orthogonal grid

as used for hydrodynamic calculations. Further details of the modelling system and the numerical method can be found in Li (2004).

MODEL RESULT

The numerical model has been tested against a range of laboratory measurements with overall good agreement, as indicated above. In the present study, the results of modelling the laboratory data from Villaret & Perrier (1992) are presented. These particular data involve waves on their own (called waves-alone) and waves combined with a co-linear current. The second case considered is the field study of Saulter *et al.* (2000) at Egmond-an-Zee (the Netherlands) for wave action in the presence of a long-shore current.

Villaret & Perrier (1992) test

Villaret & Perrier (1992) carried out a series of experiments involving waves-alone, and waves with a co-linear current above a rippled bed in a wave flume of the Laboratoire National d'Hydraulique, France. In the experiments, three ultrasonic velocimeters and an optical turbidity probe were used to measure the instantaneous horizontal velocity component and the sediment concentration. Suction samplers were also used to collect data on the wave-period-mean sediment concentrations. Three test situations were selected for the testing of the present numerical model: waves-alone, T35; waves-with-a-following-current, T36; and waves-with-an-opposing-current, T38. Details of the experimental conditions for these tests are listed in Table 1. During these tests, however, small reflections from the end of the flume were also detected, but these were typically less than 10% of the incident wave height and were not considered in the model simulation. The sediment material used in the experiments was uniform fine sand with a median diameter of 0.09 mm and a fall velocity of 7.0 mm sec⁻¹. Two-dimensional ripples were found for small wave periods (1.5 sec) but tended to become three-dimensional for longer wave periods. However, as no detailed description of the ripple geometry was presented by Villaret & Perrier (1992), the shape of the vortex ripples was represented in the model by a simple 2D hyperbolic exponential function, following Sleath (1984). It should also be noted that in the case of waves combined with a current, the ripples will move slowly in the direction of the current.

Such effects, however, have only a small influence on sediment concentrations within the water column and are neglected by using fixed ripples in the model tests.

The model was set up for each case using a numerical grid composed of 60 cells in the horizontal direction over each ripple length (in total three ripples were used) and 60 cells in the vertical direction throughout the water column. The typical time step for the tests was 1/100th of the wave period to ensure numerical stability. For the waves-alone case, T35, 20 wave cycles were required for the numerical solution to converge. However, for the waves-with-current cases, T36 and T38, the time integrations were carried out for 150 wave cycles until the difference between the solutions for successive wave cycles was small and the cycle-averaged flow discharge was close to the value in the experiments (i.e. differences less than 0.1%).

The computed results for the waves-alone case (T35) are compared with the measurements at 6 mm (about one ripple height) above the crest level at the crest and the trough in Fig. 1, including the horizontal velocities within the top panel and sand concentration within the bottom panel. It is evident from these figures that the predicted horizontal velocity at both positions agrees well with the measurements. As the comparison is made far above the ripple surface, the influence from the ripple bed on the flow velocity is not obvious in this figure. In the sediment concentration comparison panels of Fig. 1, however, two large peaks corresponding to the vortices shed during the time of flow reversal are clearly seen at both crest and trough, i.e. at around 0.25 and 1.0 sec at the crest and 0.35 and 1.1 sec at the trough. Another smaller concentration peak also is found immediately after this maximum concentration peak for every half cycle, i.e. at around 0.45 and 1.2 sec at the crest and 0.6 and 1.3 sec at the trough, which is believed to be due to the sediment trapped in vortices from neighbouring ripples passing through the observation point. Comparable features can also be found in the tests of Nakato *et al.* (1976) and in the recent experimental results of Van der Werf (2006). However, unlike the example of Nakato *et al.* (1976), the concentration time series in the present model results remain constant in the water column for a longer period between the first and second half wave cycle without obvious reduction. A third small peak is also found at around 0.75 sec during such a 'calm period', especially in the trough

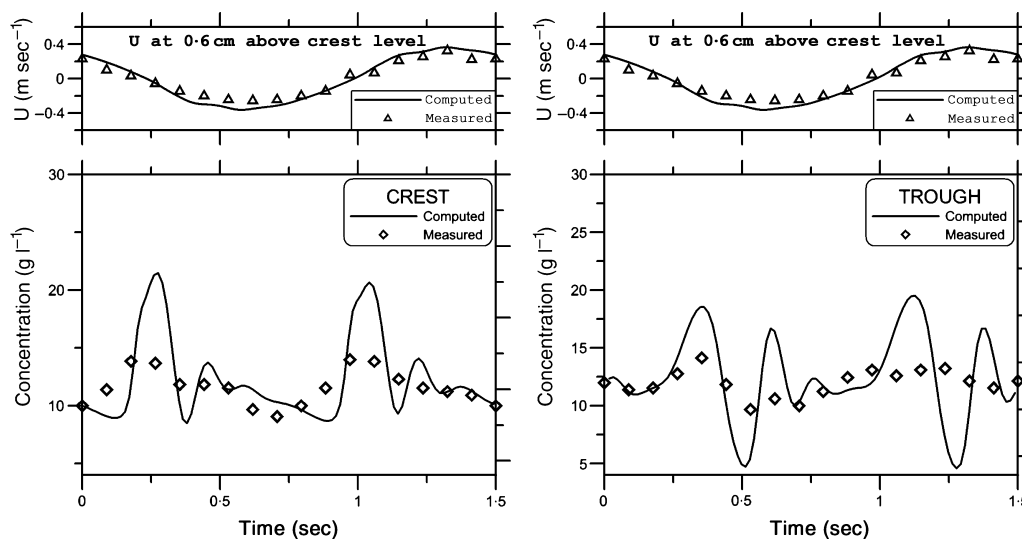


Fig. 1. Comparison of computed and measured intra-wave-period flow velocities and sediment concentrations for the waves-alone case (T35) of Villaret & Perrier (1992) at 6 mm above the crest level.

area. These differences between the Nakato *et al.* (1976) results and the present model results are believed to be largely due to the use of much finer sediment in the present tests compared with that ($d_{50} = 0.4$ mm) in Nakato *et al.* (1976). In addition, the orbital excursion for the present test is larger than one ripple length ($a = 1.5\lambda$), while in the experiments of Nakato *et al.* (1976) it is less than one ripple length ($a = 0.9\lambda$). Therefore, the stronger orbital motion of the fluid will bring more sand particles from the neighbouring ripple crest, which leads to the longer period of high sediment concentration. Comparison of the crest and trough concentration time series shows a very similar pattern, except that the peaks are delayed by some 0.25 sec because of vortex advection processes. As far as the model-data comparison is concerned, the model results follow the measurements reasonably well above the crest, although high frequency oscillations are found in the model results but not in the measurements. Above the trough, the model predicts concentration peaks ahead of the measurements while the modelled peaks corresponding to the maximum orbital stroke are absent from the measurements. This lack of correspondence is probably due to the 2D ripple geometry being used in the model. However, the limited number of sampling points throughout a wave cycle in the measurements also makes it difficult to identify any short-term variations in concentrations from the experimental data. Finally, there was a weak near-bed current in the along-tank direction during the

experiments, which will also affect the sand suspension processes and is not included in the model simulations.

The wave-period-averaged and ripple-length-averaged (along the horizontal direction) suspended sediment concentrations and the horizontal transport flux ($\mathbf{u} \times \mathbf{c}$) per unit width throughout the water column are compared with the measurements in Fig. 2. The predicted concentrations are found to decrease exponentially above the ripple crest level with the increase of distance from the ripple crest. In respect of the transport flux, a sharp onshore (positive x -direction) sand flux can be seen near the ripple crest level with a relatively smooth offshore flux higher in the water column. Such a sharp onshore peak is believed to be related to wave-induced mass transport as discussed in Davies & Villaret (1999). Above some five ripple heights (>0.05 m), the transport flux reduces to near zero for this particular test, which agrees well with the findings of Davies & Thorne (2005). During the horizontal spatial-averaging process, the concentrations below the ripple surface were not included. As a result, the sediment concentration and hence the transport flux below the crest level are obviously less than that near the crest level. By comparison with the measurements in the lowest 0.02 m region of the water column above the crest, the overall averaged errors of the predicted concentrations and sediment fluxes within Fig. 2 are less than 21% and 35% of the measured values at the crest and trough, respectively, and are considered to be satisfactory. It is also clear that the maximum

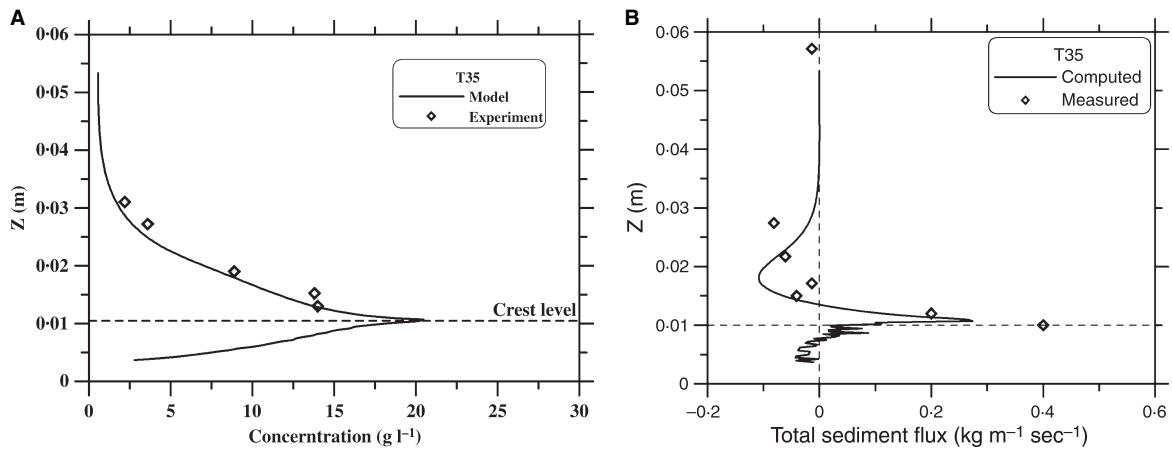


Fig. 2. Comparison of the depth-distribution of computed and measured wave-period-averaged and ripple-length-averaged sediment concentrations and total sediment flux profiles for the waves-alone case (T35) of Villaret & Perrier (1992).

onshore transport flux near the bed is under-predicted by about 25%. Apart from any three-dimensional bed geometry effects across the width of the flume, such divergences may also be related to the weak residual current flow found in the flume, as indicated above.

When a current is present, it is expected that the current flow will alter the dynamics of the vortices and the resultant sediment suspension will differ from the waves-alone case. In particular, the strength of the vortices will be asymmetrical from one half cycle to the other: a strong vortex will be generated in the current direction and a weak one in the reverse direction. In

addition, the generation of vortices around the time of flow reversal will also be affected by the current. These changes can be seen clearly in Fig. 3 which shows the computed sediment concentrations at 6 mm above the crest and trough for the case of waves-with-a-following-current (T36). At the crest, two significant large peaks can be seen corresponding to the vortex shedding from the back of the ripples immediately after the time of flow reversal (at around 0.5 and 1.2 sec). The peak in the second half wave cycle is smaller than the one in the first half cycle due to the fact that the current reinforces the vortices during the first half cycle as they

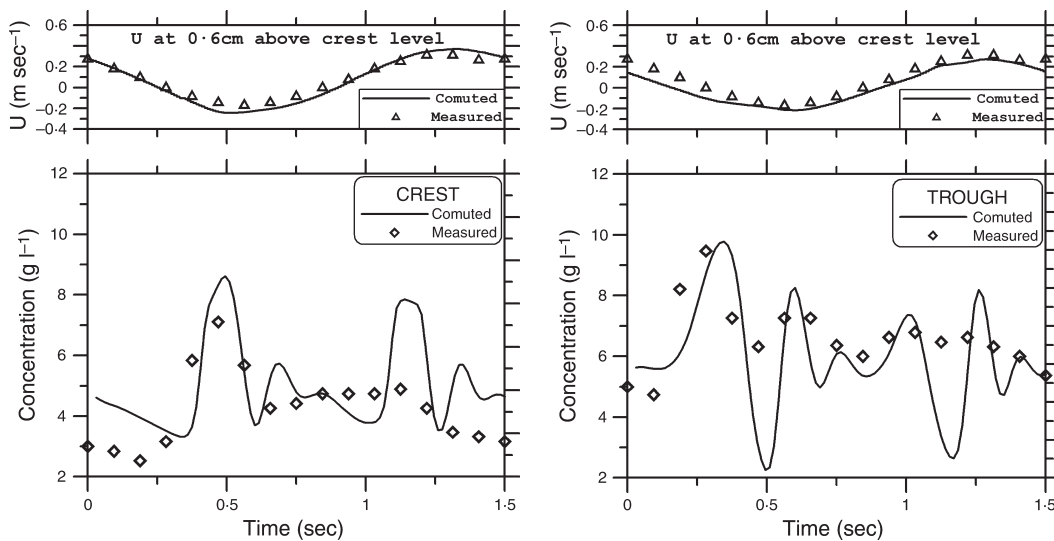


Fig. 3. Comparison of computed and measured intra-wave-period flow velocities and suspended sediment concentrations for the waves-with-a-following-current case (T36) of Villaret & Perrier (1992) at 6 mm above the crest level.

are in the same direction and, when the vortices are ejected, more sediment will be carried away from the ripple surface. The asymmetry of the vortices is seen more clearly at the trough where the peak corresponding to vortex ejection in the second half cycle (at around 1.0 sec) is much smaller compared with the one in the first half cycle (at around 0.25 sec). In a similar manner to the T35 case, a smaller peak just after the first large peak in each half cycle can still be seen above the crest (at around 0.75 and 1.3 sec), which is due to the ejected vortices from the neighbouring ripple passing through the observation point. Again, these peaks can also be observed in the trough but with a temporal offset (i.e. at around 0.6 and 1.25 sec). In addition to the asymmetry of the vortices, Fig. 3 also indicates that the concentration peaks at the crest occur after they do within the trough area; in contrast to the waves-alone case, T35 (Fig. 1), where the peaks at the crest are found to occur before those in the trough. This pattern is apparent for the first peak at around 0.5 sec above the crest in Fig. 3. The reason behind such a difference between the waves-alone case and the combined waves-with-current case is the fact that, in the combined flows, the inertia of the current suppresses the weaker upwards growth of the vortices around the time of flow reversal. As a result, the sediment cloud stays closer to the ripple surface before the ejection, unlike the waves-alone case in which the vortex can grow upwards freely. Subsequently, the cloud gives a concentration increase at the observation point in the trough area first and then moves on to give an increase at the crest. This effect can be seen more clearly in the later comparison of intra-wave sediment suspension for the waves-alone case and combined flow in Fig. 10. In both panels of Fig. 3, the general agreement between predicted and measured data is considered to be reasonable. However, the measurements in both panels (Fig. 3) are dominated by the pronounced peak in the first wave half cycle and the concentration variations in the second half wave cycle are less clear. In the same way as in the waves-alone case, the high frequency oscillation of the concentration time series from the computed results is also not found in the measurements. Another reason for these divergences is probably the asymmetrical ripple profile of the experiment, which is likely to be affected by the current, compared with the symmetrical ripple shape used in the model study. In addition to such uncertainty, the spatial three-dimensional variation of the bed geometry

and the movement of ripples also contribute to these differences between the model results and the measurements.

The wave-period-averaged and ripple-length-averaged sediment concentration profile for test T36 is compared with the measurements in Fig. 4. The overall agreements are satisfactory (error < 25%), but the over-prediction below 0.02 m and under-prediction just above this level can still be seen. By wave-period-averaging and ripple-length-averaging the total transport flux, $Q_t(z)$ per unit width can be found from the model results for this case. Similarly, the current-related transport flux $Q_c(z)$ also can be found by taking the product of the wave-period-averaged and ripple-length-averaged velocity and sediment concentration. The wave-related transport flux per unit width $Q_w(z)$, however, needs to be derived explicitly from the total transport flux and current-related one, i.e.:

$$Q_t(z) = \frac{1}{\lambda} \int_0^{\lambda} \langle uc \rangle dx \quad (6)$$

$$Q_c(z) = \frac{1}{\lambda} \int_0^{\lambda} \langle u \rangle \times \langle c \rangle dx \quad (7)$$

$$Q_w(z) = \frac{1}{\lambda} \int_0^{\lambda} [\langle uc \rangle - \langle u \rangle \langle c \rangle] dx \quad (8)$$

where $\langle \rangle$ denotes a wave-period-average operator and λ is the ripple length. These three fluxes are compared with the measurements in Fig. 5. It is

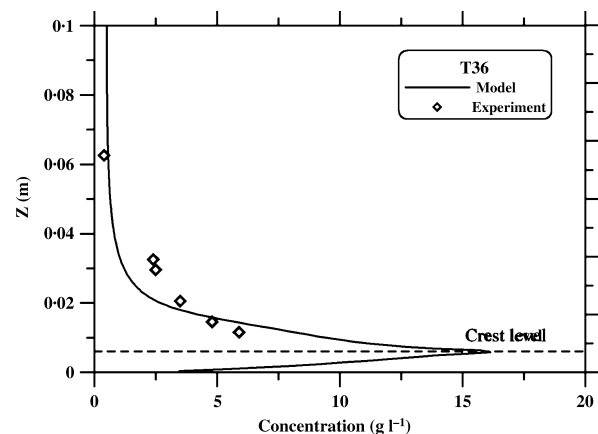


Fig. 4. Comparison of computed and measured wave-period-averaged and ripple-length-averaged suspended sediment concentrations for the T36 case of Villaret & Perrier (1992).

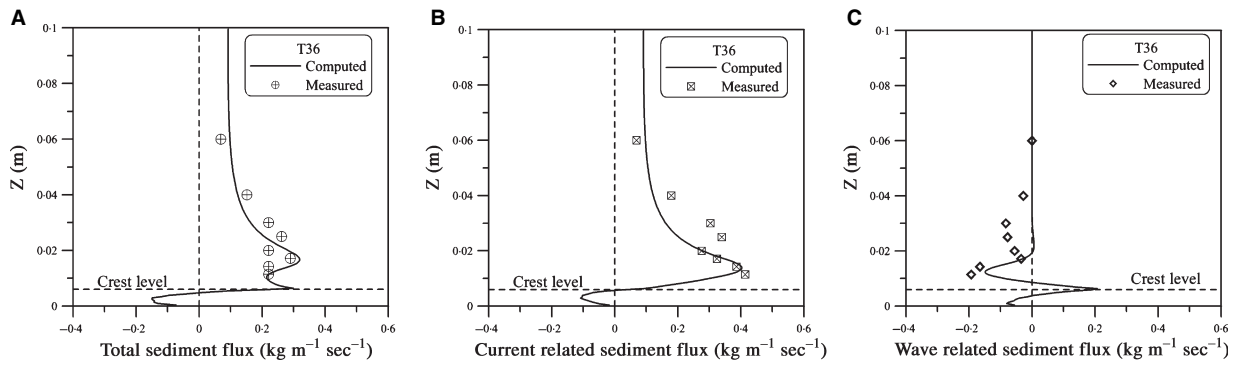


Fig. 5. Comparison of the depth-distribution of computed and measured wave-period-averaged and ripple-length-averaged total (A), current-related (B) and wave-related (C) sediment fluxes for the T36 case of Villaret & Perrier (1992).

evident that the current-related sediment flux Q_c above the ripple crest level is always directed onshore (the current direction) and is in contrast to the wave-related transport flux where a significant amount of sediment is transported offshore higher in the water column: an onshore flux only exists very close to the ripple crest level. As the wave-related transport is small compared with that of the current-related transport, the total transport flux is in the onshore direction. This result indicates that the wave oscillatory motion entrains the sediments, while the current is responsible for the net transport process in the direction of the mean flow. The wave-related transport part, therefore, can be seen as being less important in the present case. Overall, the predictions are quite reasonable when compared with the laboratory data in terms of both transport

fluxes: the error for the total transport flux being less than 20%. The wave-related flux, however, is under-predicted at around the two to three ripple heights level (0.02–0.04 m) as indicated in Fig. 5C. Such divergence is related to the over-predicted sediment concentration during the onshore flow period, as shown in Fig. 3, which leads to less offshore transport after wave-period-averaging. Apart from the uncertainties involved in the measurements, the comparison also indicates the difficulty of getting accurate wave-related transport data unless all intra-wave processes have been properly measured or predicted, particularly for the present fine sand tests, which have strong phase-lag effects.

In Fig. 6, the predicted concentration time series at the crest and trough are compared with the measurements for the case of waves-with-an-

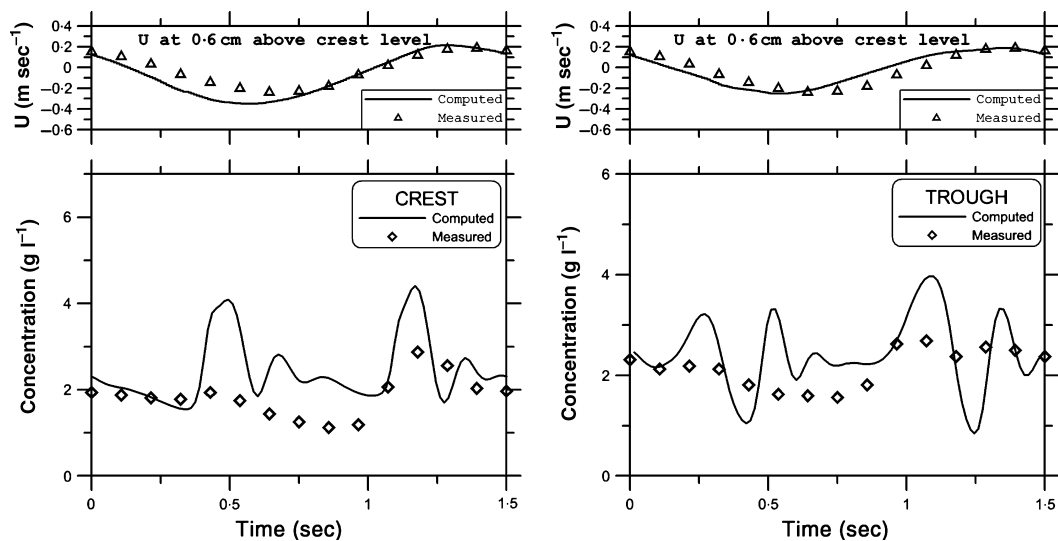


Fig. 6. Comparison of computed and measured intra-wave-period flow velocities and suspended sediment concentrations for the waves-with-an-opposing-current case (T38) of Villaret & Perrier (1992) at 6 mm above the crest level.

opposing-current (T38) at 6 mm above the crest level. The concentrations at these two locations show a very similar pattern to that noted in the case of waves-with-a-following-current (T36), which is due to the fact that the relative strength of the current to the wave orbital velocity for these two cases is comparable. The difference between the two cases lies in the opposing direction of the current in relation to the direction of the wave propagation. The concentration peaks observed in T36 at the first half cycle, therefore, correspond to those in the second half of wave cycle in T38 at both crest and trough. Because of the relatively weak orbital velocity and steady current in T38 compared with that in T36, however, the wave-period-mean value of sediment concentration in T38 is noticeably smaller than that of T36. The overall agreement between the model and measurements is not as good as that for T36. Again, this is probably related to the weak near-bed current from the wave reflections at the end of the flume, which has not been included in the model. The different ripple geometry of T38 in contrast to that in T36 may also have contributed to these differences.

The predicted wave-period-averaged and ripple-length-averaged sediment concentration distribution is also shown in Fig. 7 along with the measurements. At elevations around two ripple heights ($z > 0.02$ m), again the under-prediction is seen (see also Fig. 4). The predicted wave-period-averaged and ripple-length-averaged total sediment flux, current-related sediment flux and wave-related sediment flux throughout the water column are compared with the measurements in Fig. 8. The main observation is an obvious strong current-induced sediment transport in the offshore direction in contrast to that in the wave-with-following-current case (T36), although these two cases share very similar patterns.

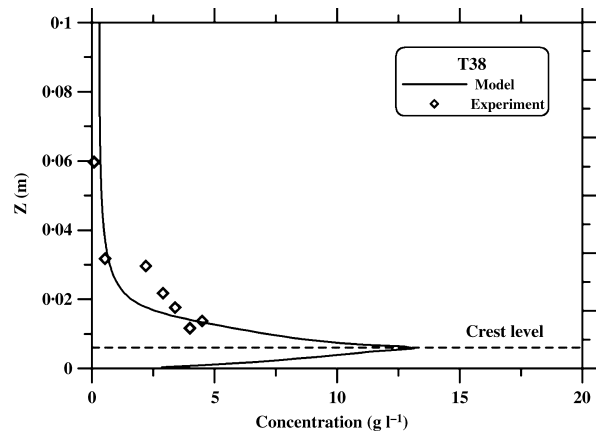


Fig. 7. Comparison of the depth-distribution of computed and measured wave-period-averaged and ripple-length-averaged suspended sediment concentration for the T38 case of Villaret & Perrier (1992).

By integrating the results in Fig. 5 and Fig. 8 over the entire depth, the modelled total suspended sediment transport rate and wave-related suspended transport rate for T36 and T38 are obtained and compared with measurements in Fig. 9. It is clear that the wave-related transport rate generally is much less than the total transport rate in both cases. For the case of waves-with-a-following-current (T36), the wave-related transport is about 10% of the total transport rate but, in the waves-with-an-opposing-current case, it contributes about 30%. As discussed above, the model seems to predict the total suspended transport rate very well for T36, although it is overestimated by 50% for T38. For wave-related transport rates, the prediction agrees with the data better for T38 than that for T36, which is under-predicted. In all cases, it should be noted that only a relatively few measured data points are available for inclusion in these comparisons.

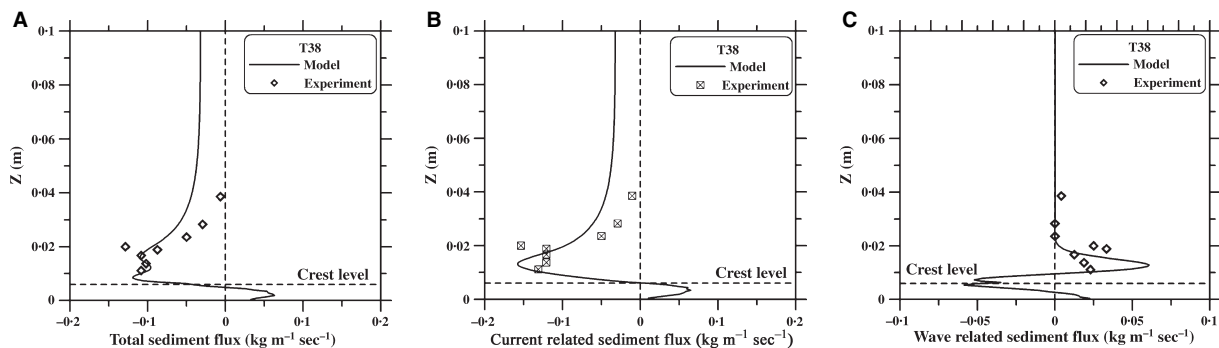


Fig. 8. Comparison of the depth-distribution of computed and measured wave-period-averaged and ripple-length-averaged total (A), current-related (B) and wave-related (C) sediment transport fluxes for the T38 case of Villaret & Perrier (1992).

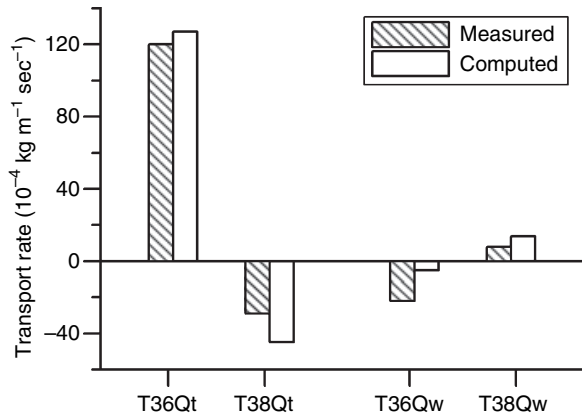


Fig. 9. Comparison of computed and measured total and wave-related suspended sediment transport rates for the cases of waves-with-a-following-current (T36) and waves-with-an-opposing-current (T38) of Villaret & Perrier (1992), Q_t is the total wave-period-averaged and ripple-length averaged suspended transport rate, Q_w is the wave-period-averaged and ripple-length-averaged suspended transport rate due to waves.

To further reveal the details of the influences of the steady current on sediment suspension, Fig. 10 compares the computed suspended sediment concentration distributions along a ripple throughout one wave cycle for the case of waves-alone, T35, and the case of waves-with-a-following-current, T36. For convenience, the starting point for the wave cycle is set at the time of the flow reversal, i.e. the flow starts to turn from the right-hand side of the ripple crest (onshore) towards the left-hand side (offshore). At the beginning of the wave cycle, a vortex at the onshore side of the crest can be observed in both cases, which has been lifted from the ripple surface with a large amount of sediment forming a cloud. As the flow accelerates towards offshore, this vortex is ejected into the water column quickly along with the sediment cloud being thrown over the crest to the offshore side, which leads to the concentration peak at the crest in the waves-alone case, and the filling up of the trough area on the offshore side until the phase time equals a quarter of the wave cycle (90°), causing the concentration peak at the trough in the waves-alone case. Due to effects from the current, the sediment cloud in the waves-with-a-following-current case stays closer to the ripple surface than that in the waves-alone case. The sediment cloud therefore passes the observation point (0.6 mm above crest level) in the trough area first and then rises up to that above the crest, which leads to the concentration peaks at the trough first and then the crest. As

the flow starts to decelerate, and then change direction and accelerate towards onshore, the sediment cloud is lifted up from the ripple trough area and propagates into the water column in both cases (wave phase 150° – 210°). However, in the waves-with-a-following-current case, the sediment cloud is smaller than that in the previous half cycle and the current carries the cloud over the ripple crest earlier than is found for the waves-alone case (210°). Then the flow field is dominated by the current in the waves-and-current case with the vortices formed on the onshore side of the ripple occupying the trough zone for a longer period of time than in the waves-alone case.

After horizontal integration, the sediment entrainment process is depicted in Fig. 11, in which the vertical distribution of ripple-length-averaged sediment concentration is plotted against time for all three test cases, T35, T36 and T38, respectively. The ripple crest level is indicated by the solid lines across the bottom of the figure and the corresponding orbital-velocity-time-history is plotted at the top of the figure. In all three cases, four peaks are clearly seen around two ripple heights (0.014 m) in the water column, marked as A, B, C and D. The peaks A and B correspond to the vortex ejection events just after flow reversal, which are more significant and affect the sediment concentration distribution further away from the bed. The relatively smaller peaks of C and D are due to the large sediment cloud in the ripple trough region just before maximum flow. It can be seen that most of the vortex shedding effects are restricted to around two to three ripple heights (below 0.02 m) for these three cases. However, unlike the oscillatory flow above a flat bed, the concentration peaks are dominated by the large sediment cloud introduced by vortex shedding while the vertical mixing process by turbulence is relatively less important. Compared with the waves-alone case, T35, the influences of the four peaks in T36 and T38 are different due to the presence of the current. In T36, the peaks of the first half cycle roughly follow the same evolution as in the waves-alone case except for the fact that they are held closer to the bed. However, in the second half cycle, in which the wave is propagating with the current, the peaks appear to be weak and the impact on suspension is much less significant higher in the water column compared with the waves-alone case. A similar pattern can also be seen in the T38 case.

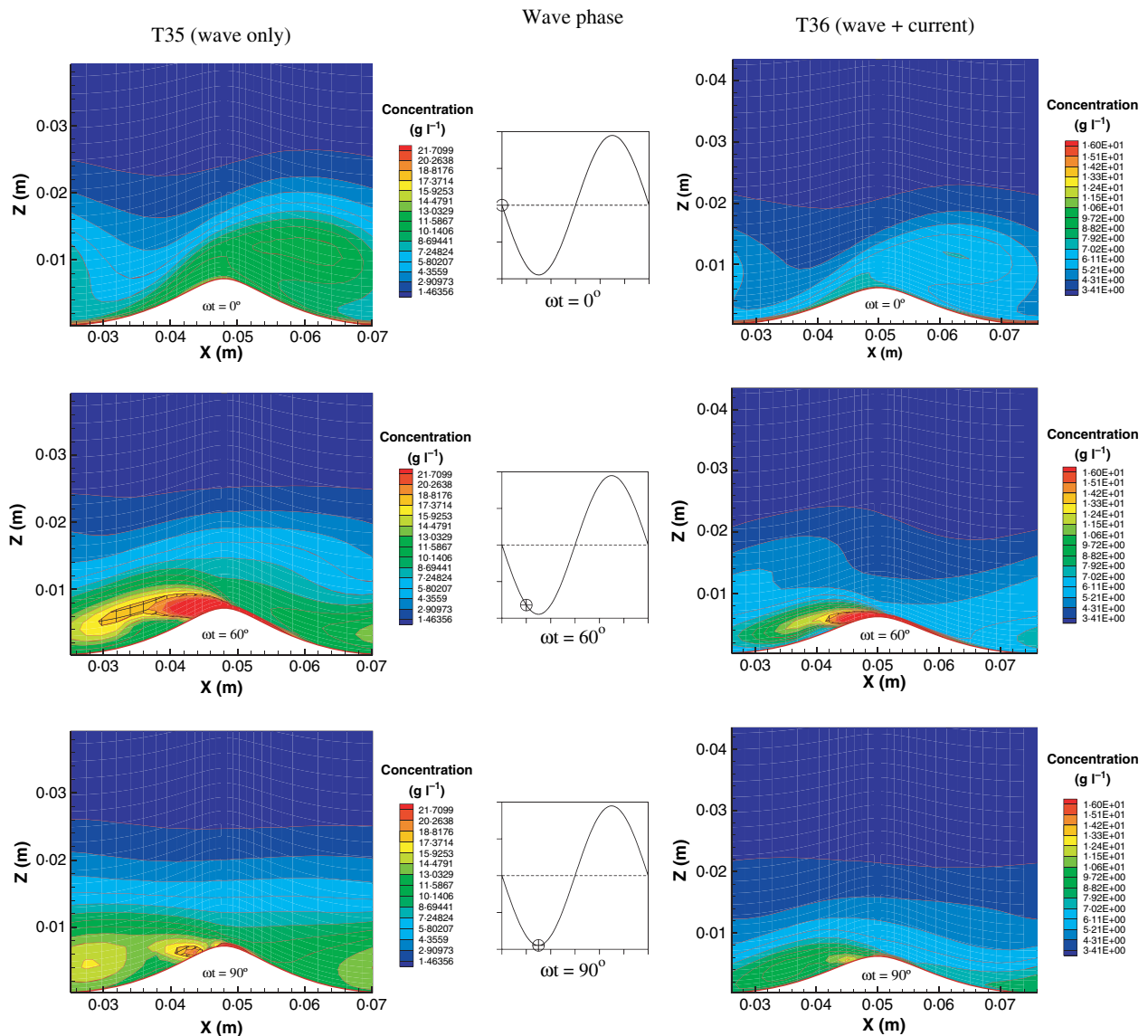


Fig. 10. Comparison of computed intra-wave-period sediment concentrations for the cases of waves-alone (T35) and waves-with-a-following-current (T36) of Villaret & Perrier (1992).

Field test, Saulter *et al.* (2000) test

The model results represented above were carried out in a two-dimensional (horizontal–vertical) domain with the assumption that the flow condition in the third direction (y) was uniform. In nature, however, the flow in the near-shore zone is more likely to be three-dimensional with waves propagating at an angle to the tidal or wave-induced flows. Therefore, it is necessary for the numerical model to be able to handle the general flow situation in which waves interact with a current at any given angle.

To further test the model under these complex flow conditions, and to examine the correspond-

ing sediment entrainment process, the model was used to simulate a set of field measurements obtained by Saulter *et al.* (2000). The experiments were made on a multiple-barred, dissipative beach at Egmond-an-Zee (the Netherlands) in October/November 1998 over a six-week period. Repeated storm events were observed during the experimental period. All the measurements were made in the inter-tidal zone and thus observations were made around the high water periods of individual tides. Hydrodynamic and suspended sediment concentration parameters were measured using a synchronous logger for investigation of transport of sediments (SLOT) system, which incorporates a pressure transducer (PT), electro-

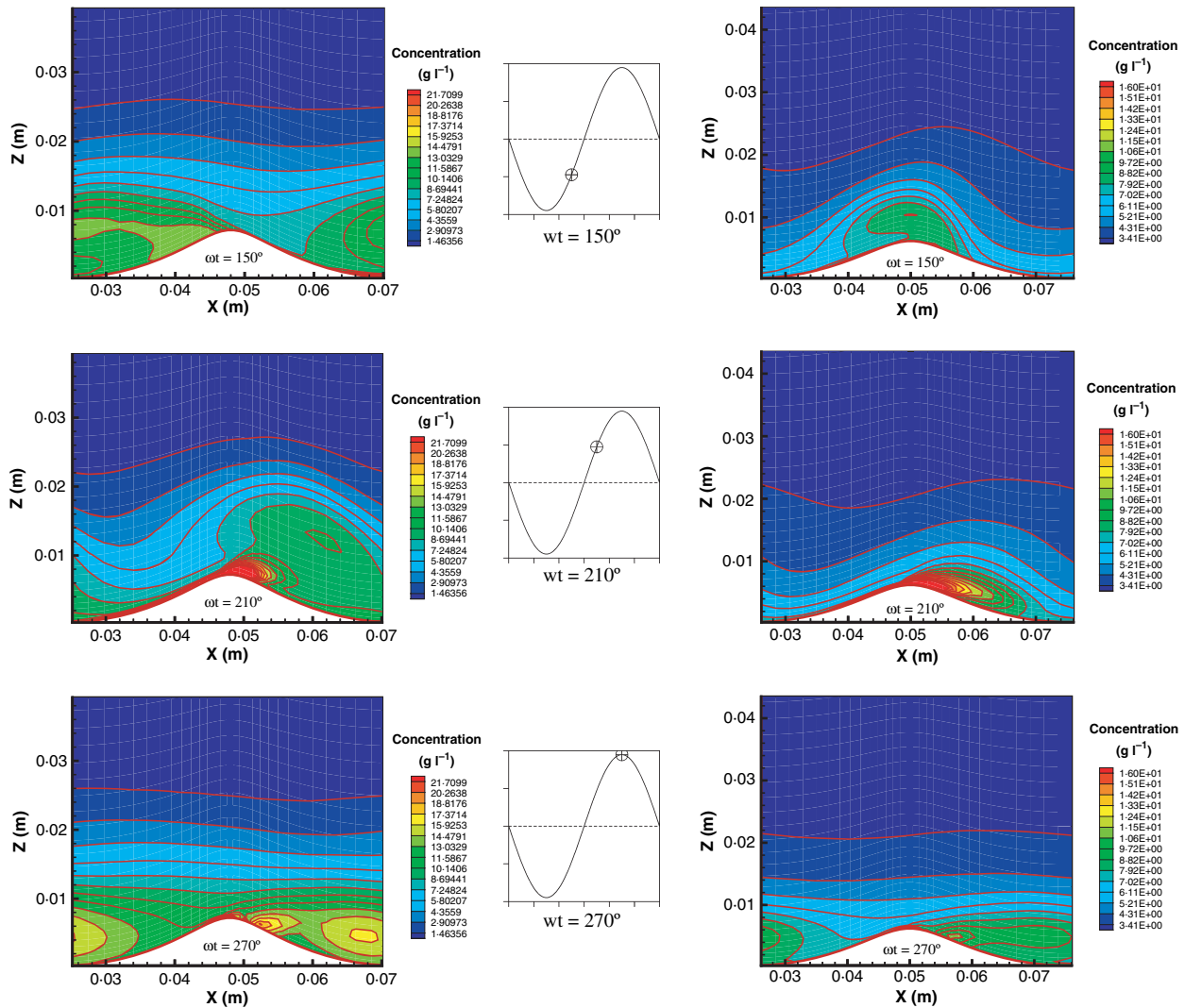


Fig. 10. (Continued)

magnetic current meter (EMCM) and optical backscatter sensor (OBS). The bedform characteristics were measured by two instruments: a rotating side scan sonar with a 1.2 MHz sampling rate (SRILS) and a sonar altimeter with a 2 MHz sampling rate.

One experiment condition (RUN1), which appears to have less wave breaking effects and weak cross-shore undertow flow, was selected for model testing and the details are listed in Table 2. The waves were found to propagate towards the shoreline with ripples developed in the same direction (Fig. 12). A weak cross-shore current was found together with a stronger current in the long-shore direction. The instruments were deployed at around 0.18 m above a long period (>10 h) mean bed level. Time series of suspended sediment concentration and flow velocities were recorded at the same measuring point. During the

experiment, the median size of the near-bed sediment particles at the measuring site was found to be 0.3 mm.

The numerical model was set up according to the measured conditions with variations in all three dimensions. Two side boundaries in the long-shore (x) and cross-shore (y) directions were set as periodic boundaries. On the ripple surface the velocity was specified by a no-slip condition. At the top of the computational domain, a no-shear stress condition was used such that the gradient of the velocities and turbulence characteristics was assumed to be zero. The same top and bottom conditions as in the previous 2D cases were used for sediment concentration calculations.

To resolve the computational grid system, orthogonal grids were generated first along the cross-shore direction (x - z domain) and then the

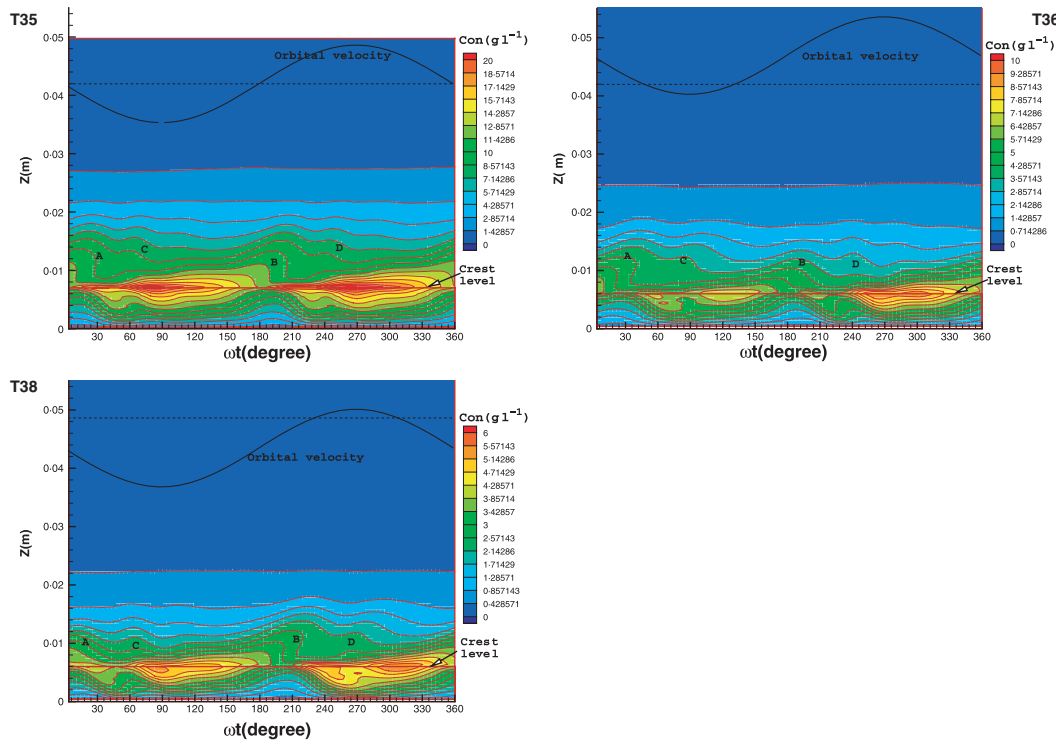


Fig. 11. Comparison of computed ripple-length-averaged sediment concentrations for the cases of waves-alone (T35), waves-with-a-following-current (T36) and waves-with-an-opposing-current (T38) of Villaret & Perrier (1992).

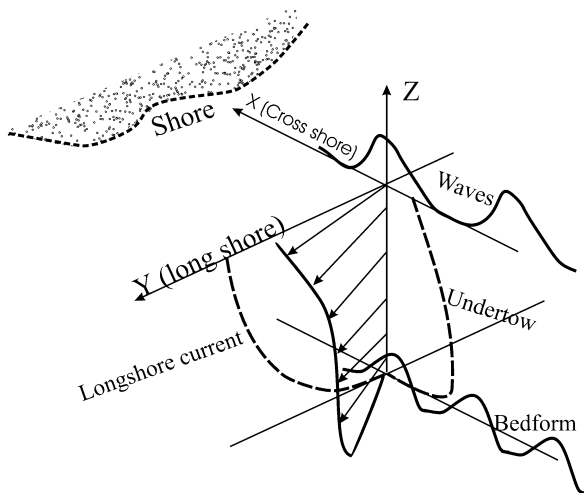


Fig. 12. Schematic representation of flow conditions for the Saulter *et al.* (2000) three-dimensional wave-current interaction test case.

generated grid was uniformly distributed along the long-shore (*y*) direction. It is assumed, therefore, that the ripples are long-crested. Two vortex ripples were placed in the cross-shore direction with the ripple shape prescribed by a hyperbolic exponential function, as in the earlier sections above, with the same characteristics as in the measurements. For each ripple, 60 grid

cells were used along the *x* direction and 60 grid cells with variable sizes in the *z* direction. In the *y* direction a total of 20 computational cells were used to resolve the flow variations in the long-shore direction for a distance of 10 ripple lengths.

Due to the small depth-mean onshore current velocity compared with the wave orbital velocity amplitude (<7%), the flow field in the cross-shore direction was assumed to be dominated by the waves and the weak steady current was ignored. This approach has the advantage that the iterations required in the model in order to calculate the surface pressure gradient associated with the steady current, see also Li (2004), were only required in the long-shore (*y*) direction after time integration over each wave cycle. This approach considerably reduces the total computational time compared with that for the case with iterations being carried out in both cross-shore and long-shore directions. However, for a general 3D case, the surface pressure drop, i.e. the current-driving force, has to be found in both the *x* and *y* directions, as demonstrated by Andersen & Faraci (2003). According to the experimental condition, the near-bed orbital velocity was simulated using second order Stokes' theory. The effect of wave breaking is ignored as

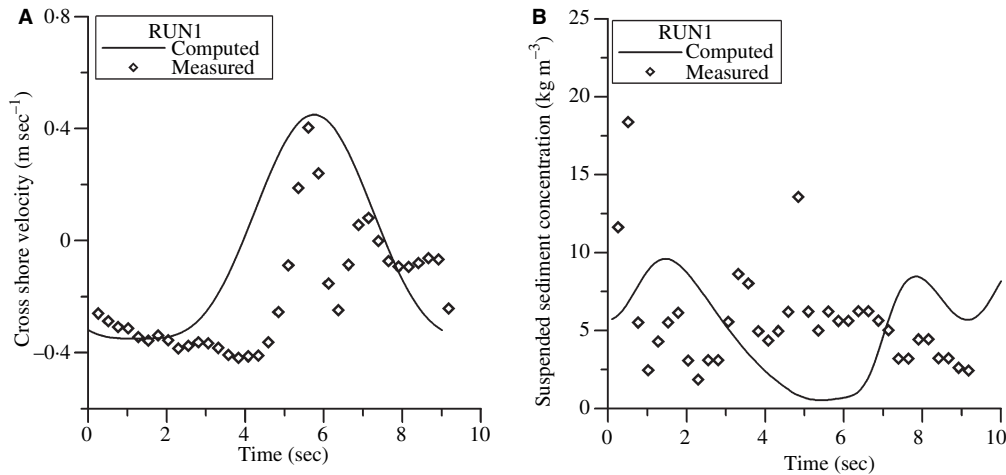


Fig. 13. Comparison of intra-wave-period computed and measured cross-shore velocity (A) and suspended sediment concentrations (B) at 0.18 m above the bed level for the Saulter *et al.* (2000) test case.

are the vertical velocities from the surface wave motion.

The computation was integrated forward with a time step of 1/100th of the wave period for 50 wave cycles until the flow field had converged so that the differences between two adjacent wave cycles were small and the computed flow rate in the y direction agreed closely with the measurements (i.e. <0.1%).

The computed time history of cross-shore velocity at 18 cm above the bed level is compared with the Saulter *et al.* (2000) measurements in Fig. 13A. It can be seen that the prediction follows the measurements reasonably well in terms of the maximum onshore and offshore flow velocities. However, the predicted values begin to increase towards the onshore direction much earlier than the measured data. Another important aspect of the wave dynamics that is also missing in the present study is the effect of wave breaking of a series of random waves, which would have considerable impact on the flow velocity and sediment concentration distribution. Because the measurements were made far above the bed, the effects from the ripples are not seen as clearly as in earlier laboratory tests. More detailed measurements would, therefore, be useful to reveal the flow field within the boundary layer and help to establish the precision and usefulness of the present model.

The computed suspended sediment concentrations at 0.18 m above the bed are also compared with the measured values in Fig. 13B. It should be noted in viewing these results that the observation point is well above the ripple surface, so that considerable mixing has occurred compared

with the release time of sediment from the bed by the vortices. The model produces a similar wave-period-mean concentration value as the measurements (<15% error). The two concentration peaks corresponding to the maximum onshore and offshore flow velocities are also evident in the computed results. The measured data, however, shows a more scattered pattern than the model with several sharp peaks which are not seen in the predictions. These peaks are most probably related to wave breaking events and wave grouping and randomness during the experiments. In addition, it should be noted that the errors involved in the field measurements are particularly difficult to quantify, which also contributes to the above discrepancies.

To reveal more details of sediment suspension under 3D combined flows, Fig. 14 shows the flow field and suspended sediment concentrations over ripples during the wave cycle. It can be seen that the flow near to the ripple crest is controlled by the vortex ejection and shedding. However, unlike the waves with in-line current or waves-alone cases, the vortex generated during the time of flow reversal is not simply lifted away from the bed into the water column; it appears to stay low, close to the ripple trough, and is then rolled up with the long-shore current and dissipated into the water column before the flow begins to accelerate in the following half wave cycle. However, the corresponding suspended sediment concentration seems to be less affected by the long-shore current (Fig. 14). The major feature of the sediment entrainment process is fairly similar to the situation with only waves present above a rippled bed, with the large vortex eroding

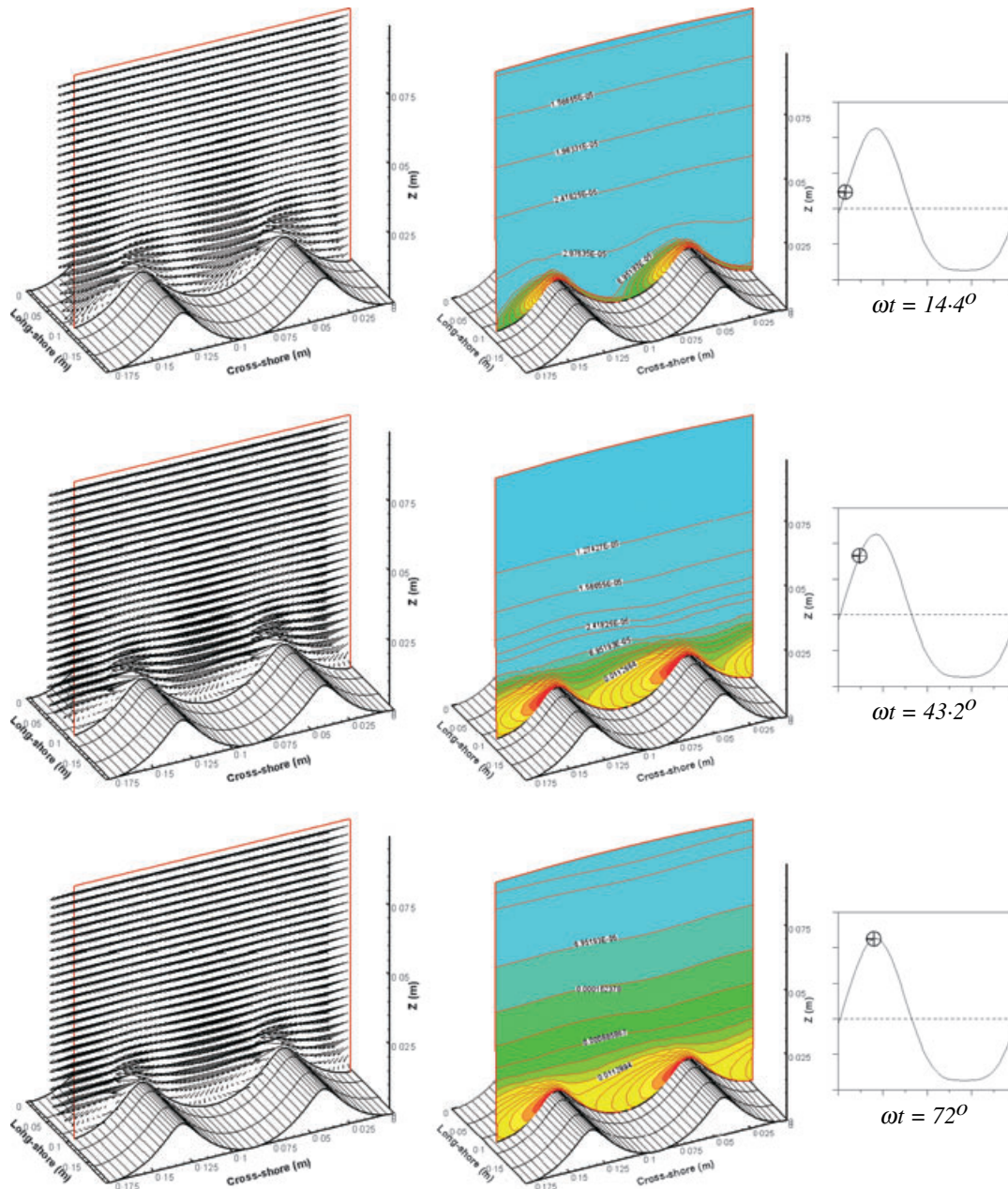


Fig. 14. Computed depth-distribution of flow velocities and suspended sediment concentrations above the ripple bed surface for the first half of a wave cycle for the Saulters *et al.* (2000) test case.

sediment and then being ejected into suspension just after the flow begins to reverse. The sediment cloud also tends to be very close to the ripple crest level. Further above the bed, the concentration becomes very small compared with that close to the bed level; to a large extent, this is due to the fairly large sediment size in this particular case. Meanwhile, because the long-shore current was assumed to be steady, the concentration gradient along the y direction is found to be very small once the solution has converged. When a three-

dimensional ripple profile is involved, the sediment concentration is expected to have some spatial variation in the long-shore direction as well, which may lead to different sediment concentration distributions.

The wave-period-averaged and ripple-length-averaged cross-shore and long-shore velocities, and the corresponding sediment concentration distributions are shown in Fig. 15. As expected, the cross-shore velocity is dominated by the wave-induced flows and the overshoot above the

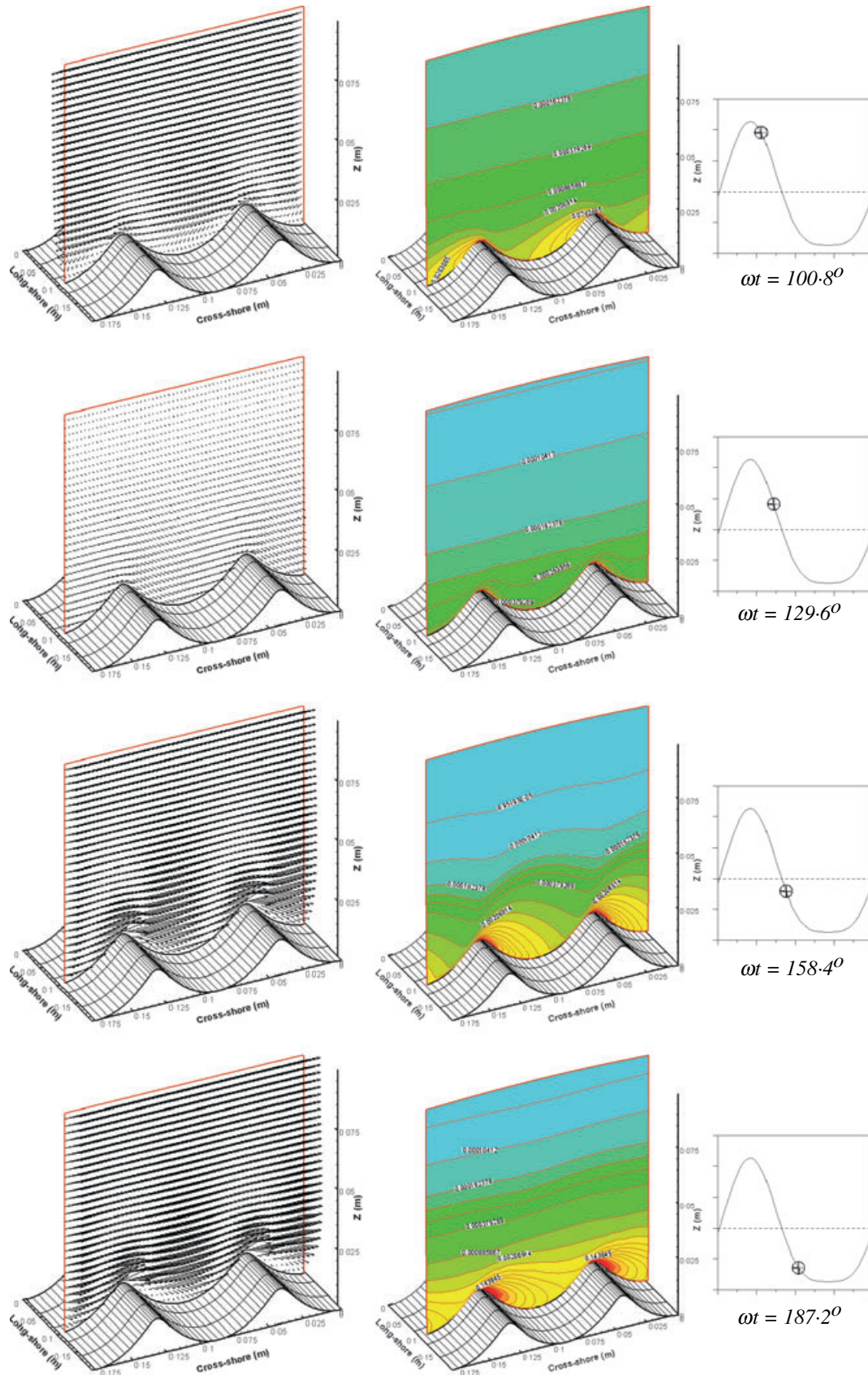


Fig. 14. (Continued)

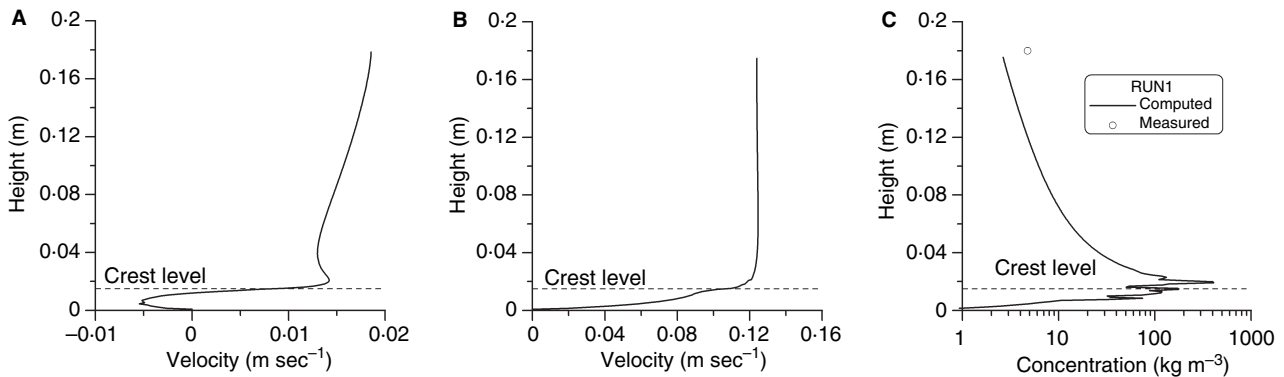


Fig. 15. Computed depth-distribution of wave-period and ripple-length-averaged cross-shore (A) and long-shore (B) velocity profiles, and sediment concentrations (C) for the ripple bed test case of Saulter *et al.* (2000).

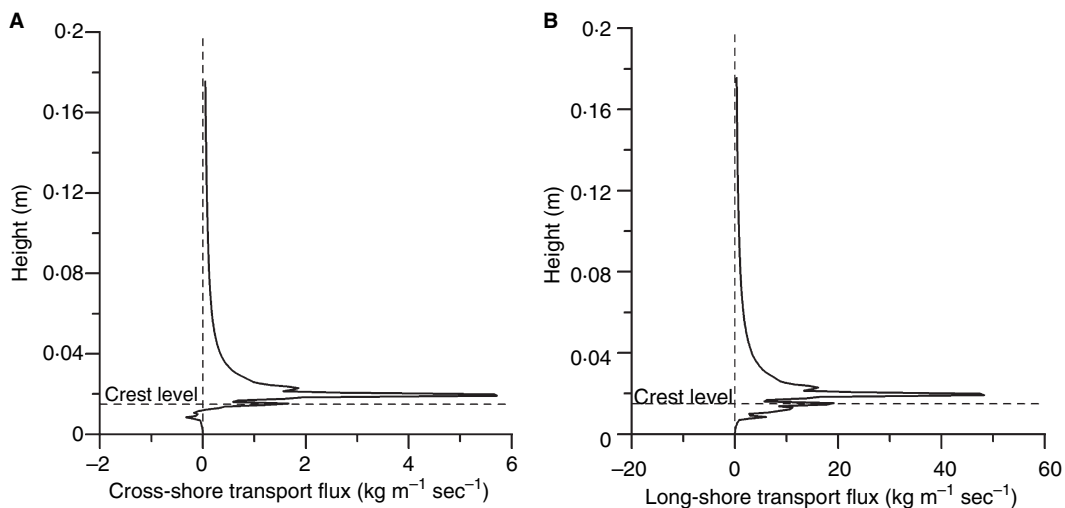


Fig. 16. Computed depth-distribution of wave-period and ripple-length-averaged cross-shore (A) and long-shore (B) sediment transport fluxes for the Saulter *et al.* (2000) test case.

ripple crest level is clearly evident. The long-shore current, however, maintains roughly a logarithmic pattern above the ripple crest level. For situations in which the current intersects the waves at an arbitrary angle, both cross-shore and long-shore velocities in the wave boundary layer would be expected to be different from those above. The wave-period-averaged and ripple-length-averaged sediment transport flux in both cross-shore and long-shore directions are also presented in Fig. 16. It is clear that the cross-shore transport, which is mainly due to waves, is only a small portion of that in the long-shore direction. In a similar manner to the co-linear waves and current case in the Villaret & Perrier (1992) test, T36, the peak in wave-related transport flux occurs just above the ripple crest and is seen clearly. However, the transport in the offshore direction is not evident. This is partly

due to the larger grain size involved in this particular test, as well as the fact that the waves intersect at right angles with the current. It should be borne in mind that the results presented herein do not include wave streaming and undertow effects, which are often important components of surf zone dynamics. With the presence of an undertow, it is generally expected that the net sediment transport will be offshore close to the bed (Fredsoe & Deigaard, 1992).

CONCLUSIONS

In order to investigate sediment transport processes above rippled beds in the coastal environment, a numerical model has been developed and tested against a number of experimental tests. Compared with the laboratory experiments of Villaret &

Perrier (1992), the model has shown agreement with the measurements for situations involving waves-alone, waves-with-a-following-current, and waves-with-an-opposing current. The model results also indicate the considerable influences from a steady current on the detailed intra-wave flow patterns and the vortex dynamics close to the ripple surface. It appears that the waves are responsible for suspending sediment into the water column, while the current is able to transport the sediment both horizontally and vertically across the water column. The presence of the current also affects the strength of the vortex formed during the accelerating and decelerating parts of the wave cycle which in turn affects the corresponding sediment suspension process.

To study sediment suspension under combined waves with a current at right angles to the direction of wave propagation, the numerical model also was applied to field data in which a long-shore current interacted with waves in the cross-shore direction above a rippled bed (Saulter *et al.*, 2000). Model results for a simplified set of field conditions were compared with the measurements at the top of the wave boundary layer and showed realistic values for both flow velocities and sediment concentrations during the wave period. The complex 3D flow structure appears to affect the vortex shedding process immediately after the time of flow reversal. Due to the interaction of the waves and current field at right angles, the intra-wave period sediment concentration distributions show a similar pattern to the 2D test cases of Villaret & Perrier (1992). The sediment transport higher in the water column is, however, dominated by the long-shore current. A more detailed study of the sediment suspension under combined waves and currents at various angles clearly would be useful to quantify the influences from the current on the sediment transport process within the boundary layer. Such a study also would also require a much greater quantity of field data in order to judge the usefulness of the computer model.

ACKNOWLEDGMENTS

This work was partly supported by the Engineering and Physical Sciences Research Council (UK) under contract number GR/R83545 and GR/R96967. The authors also would like to thank all the referees in particular Professor Paul Carling for their helpful comments in the preparation of the manuscript.

REFERENCES

- Andersen, K.H. and Faraci, C. (2003) The wave plus current flow over vortex ripples at an arbitrary angle. *Coast. Eng.*, **47**, 431–441.
- Barr, B.C., Slinn, D.N., Pierro, T. and Winters, K.B. (2004) Numerical simulation of turbulent, oscillatory flow over sand ripples. *J. Geophys. Res.*, **109**, doi: 10.1029/2002JC001709.
- Blondeaux, P. and Vittori, G. (1991) Vorticity dynamics in an oscillatory flow over a rippled bed. *J. Fluid Mech.*, **226**, 257–289.
- Davies, A.G. and Thorne, P. (2005) Modelling and measurement of sediment transport by waves in the vortex ripple regime. *J. Geophys. Res.*, **110**, doi: 10.1029/2004JC002468.
- Davies, A.G. and Villaret, C. (1999) Eulerian drift induced by progressive waves above rippled and very rough beds. *J. Geophys. Res.*, **104**(C1), 1465–1488.
- Dvinsky, A.D. (1987) FLUENT/BFC: a general purpose fluid flow modelling program for all flow speeds. In: *Numerical Methods in Laminar and Turbulent Flow* (Eds C. Taylor, W. Habashi and M. Hafez) **5**(Part 1), 137–148. Prineridge press, Swansea, UK.
- Eidsvik, K.J. (2006) Large scale modelling of oscillatory flows over a rippled bottom. *Cont. Shelf Res.*, **26**, 318–337.
- Engelund, F. and Fredsøe, J. (1976) A sediment transport model for straight alluvial channels. *Nord. Hydrol.*, **7**, 293–306.
- Faraci, C. and Foti, E. (2001) Evolution of small regular patterns generated by waves propagating over a sandy bottom. *Phys. Fluids*, **13**, 1624–1634.
- Fredsøe, J. and Deigaard, R. (1992) *Mechanics of Coastal Sediment Transport*. World Scientific, Singapore.
- Fredsøe, J., Andersen, K.H. and Summer, B.M. (1999) Wave plus current over a ripple-covered bed. *Coast. Eng.*, **38**, 177–221.
- Kim, H., O'Connor, B.A., Kim, T.H. and Williams, J.J. (2000) *Suspended Sediment Concentration over Ripples*. Coastal Engineering 2000 (ICCE), Sydney, Australia, ASCE, pp. 2873–2885.
- Lauder, B.E. (1989) Second-moment closure: present...and future? *Int. J. Heat Fluid Flow*, **10**, 282–300.
- Leonard, B.P. (1979) A stable and accurate convection modelling procedure based on quadratic upstream interpolation. *Comput. Meth. Appl. Mech. Eng.*, **19**, 59–98.
- Li, M. (2004) Micro-modelling of suspended sediment transport over bedforms. PhD thesis, Department of Civil Engineering, The University of Liverpool, Liverpool.
- Li, M. and O'Connor, B.A. (2000) *Effective Roughness of Bedforms, Hydraulic Engineering Software, VIII*. WIT Press, Lisbon, Portugal, pp. 143–152.
- Li, M., Pan, S. and O'Connor, B.A. (2006) Modelling coastal boundary layer flows over typical bed-forms. *Proc. Inst. Civ. Eng. Marit. Eng.*, **159**(MA1), 9–24.
- Malarkey, J. and Davies, A.G. (2002) Discrete vortex modelling of oscillatory flow over ripples. *Appl. Ocean Res.*, **24**, 127–145.
- Meyer-Peter, E. and Müller, R. (1948) Formulas for bed-load transport. *Rep. 2nd Meet. Int. Assoc. Hydraul. Struct. Res.*, Stockholm, pp. 39–64.
- Nakato, T., Locher, F., Glover, J. and Kennedy, J. (1976) Wave entrainment of sediment from rippled bed. *J. Waterw. Port Coast. Ocean Div. ASCE*, **103**(WW1), 83–99.
- O'Donoghue, T. and Clubb, G. (2001) Sand ripples generated by regular oscillatory flow. *Coast. Eng.*, **44**, 101–115.

- Sato, S., Uehara, H. and Watanabe, A.** (1986) Numerical simulation of the oscillatory boundary layer flow over ripples by a k-e turbulence model. *Coast. Eng. Jpn.*, **29**, 65–78.
- Saulter, A., Russell, P. and Huntley, D.** (2000) *The Effect of Bed Forms on Coastal Sediment Transport*. Coastal Engineering 2000 (ICCE), Sydney, Australia, ASCE, pp. 2627–2685.
- Sisternans, J.** (2002) *Graded Sediment Transport by Non-breaking Waves and a Current*. Communications on Hydraulic and Geotechnical Engineering, Faculty of Civil Engineering and Geosciences, DUT, Delft, p. 205.
- Sleath, J.F.A.** (1984) *Sea Bed Mechanics*. Wiley Interscience Publication, New York.
- Thorne, P., Williams, J. and Davies, A.** (2002) Suspended sediments under waves measured in a large-scale flume facility. *J. Geophys. Res.*, **107**(C8), doi: 10.1029/2001/JC000988.
- Van der Werf, J.** (2006) Sand transport over rippled beds in oscillatory flow. PhD Thesis, University of Twente, Twente, the Netherlands.
- Van Rijn, L.** (1993) *Principles of Sediment Transport in Rivers, Estuaries and Coastal Seas*. Aqua Publication, Amsterdam, the Netherlands.
- Villaret, C. and Perrier, G.** (1992) *Transport of Fine Sand by Combined Waves and Current: An Experimental Study*. Direction Des Etudes et Recherches, Electricite de France, 81 pp.
- Watanabe, Y., Matsumoto, S. and Saeki, H.** (2003) Three-dimensional boundary layer flow over ripples. *Proceedings of Coastal Sediments 03, East Meets West Productions*, Clearwater, FL, USA.

Manuscript received 22 August 2006; revision accepted 14 May 2007